ADVANCED ELECTRONIC MATERIALS
www.advelectronicmat.de

Benchmarking β-Ga_2O_3 Schottky Diodes by Nanoscale Ballistic Electron Emission Microscopy

Renato Buzio, Andrea Gerbi, Qiming He, Yuan Qin, Wenxiang Mu, Zhitai Jia,* Xutang Tao, Guangwei Xu, and Shibing Long**

Monoclinic beta-phase gallium oxide (β-Ga_2O_3) is an ultrawide-bandgap semiconductor, intensively studied as a viable candidate for next-generation power electronics, optoelectronics, and extreme environment electronics. Schottky contacts to β-Ga_2O_3 are of paramount importance to this end; however, they are not yet fundamentally understood. Intrinsic sources of interfacial disorder, including oxygen-related defects and extrinsic fabrication factors, are thought to greatly determine the properties of such contacts, for example by originating Fermi level pinning and causing patches with different Schottky barrier heights (SBHs). Ballistic electron emission microscopy (BEEM) is used to probe band bending and interfacial inhomogeneity at the nanoscale for prototypical Au/ and Pt/(100)β-Ga_2O_3 single crystal Schottky barrier diodes. It is shown that SBH fluctuations amount to 40–60 meV under vacuum, occurring over length scales of tens of nanometers. Furthermore, a remarkable SBH modulation of ≈0.2 eV takes place upon exposure of devices from vacuum to ambient air. Such findings—better obtained by BEEM than by macroscale approaches—point to the existence of an ubiquitous inhomogeneous interfacial layer, controlling band bending and ambient sensitivity via oxygen ionosorption and interface redox chemistry. This study ascribes a key role to interfacial oxygen vacancies, and has practical implications for transport modelling and interface engineering.

1. Introduction

Monoclinic beta-phase gallium oxide (β-Ga_2O_3) is a relatively new material among ultra wide bandgap semiconductors, showing outstanding properties such as chemical/thermal stability up to 1400 °C, bandgap of ≈4.8 eV, high transparency in the deep UV and visible wavelength regions, and a theoretical breakdown field of ≈8 MV cm^{-1} that greatly exceeds that of SiC and GaN.[1,2] The possibility for β-Ga_2O_3 to become a suitable platform for novel applications in power electronics, optoelectronics, and sensing strongly relies on understanding and control of the interfacial properties at metal contacts, both of Ohmic and Schottky type. In particular Schottky barrier diodes (SBDs) between large work function metals (e.g., Au, Pt, Ni, Cu) and β-Ga_2O_3 attract great attention, being a fundamental building block in several proof-of-concept devices and applications (ultra-high power rectifiers and metal-oxide–semiconductor field-effect transistors, deep UV photodetectors, photocatalists, gas sensors, transparent electronic devices).[1–3]

So far, most of the SBH values at metal/β-Ga_2O_3 interfaces were reported to lie in the range between ≈1.0 and 1.5 eV.[3–17] Such substantial scattering reflects the interplay of intrinsic and extrinsic sources of interfacial disorder, due to materials' quality and fabrication details. Schottky junctions do not obey the Schottky–Mott limit,[7] rather surface states, defect states, or metal-induced gap states are thought to have a prominent role on the barrier formation mechanism.[6] Recently, there have been evidences that the SBH critically depends on the oxygen partial pressure during metallization.[5–7] In fact, metal deposition at room-temperature (RT) under high oxygen partial pressure rises the SBH by overall ≈0.5–0.8 eV compared to a low oxygen environment, due to enhanced interfacial oxidation and increased work function of the metal oxide.[5–7] On one hand, this fact indicates that oxygen exchange reactions at the Schottky interface are highly active at temperatures far below the activation energy for migration of bulk oxygen vacancies (≈900 °C),[18] as already reported for other oxide semiconductors.[19] On the other hand, it suggests that β-Ga_2O_3 Schottky junctions might be easily (and unintentionally) reduced at contact formation, undergoing Fermi Level (FL) pinning by

Dr. R. Buzio, Dr. A. Gerbi
CNR-SPIN
C.so F.M. Perrone 24, 16152 Genova, Italy
E-mail: renato.buzio@spin.cnr.it
Q. He, Y. Qin
Key Laboratory of Microelectronics Devices and Integration Technology
Institute of Microelectronics of Chinese Academy of Sciences
100029 Beijing, China
Dr. W. Mu, Prof. Z. Jia, Prof. X. Tao
State Key Laboratory of Crystal Materials and the Key Laboratory of Functional Crystal Materials and Device
Shandong University
250100 Jinan, China
E-mail: z.jia@sdu.edu.cn
Dr. G. Xu, Prof. S. Long
The School of Microelectronics
University of Science and Technology of China
230026 Hefei, China
E-mail: shibinglong@ustc.edu.cn
The ORCID identification number(s) for the author(s) of this article can be found under https://doi.org/10.1002/aelm.201901151.

DOI: 10.1002/aelm.201901151

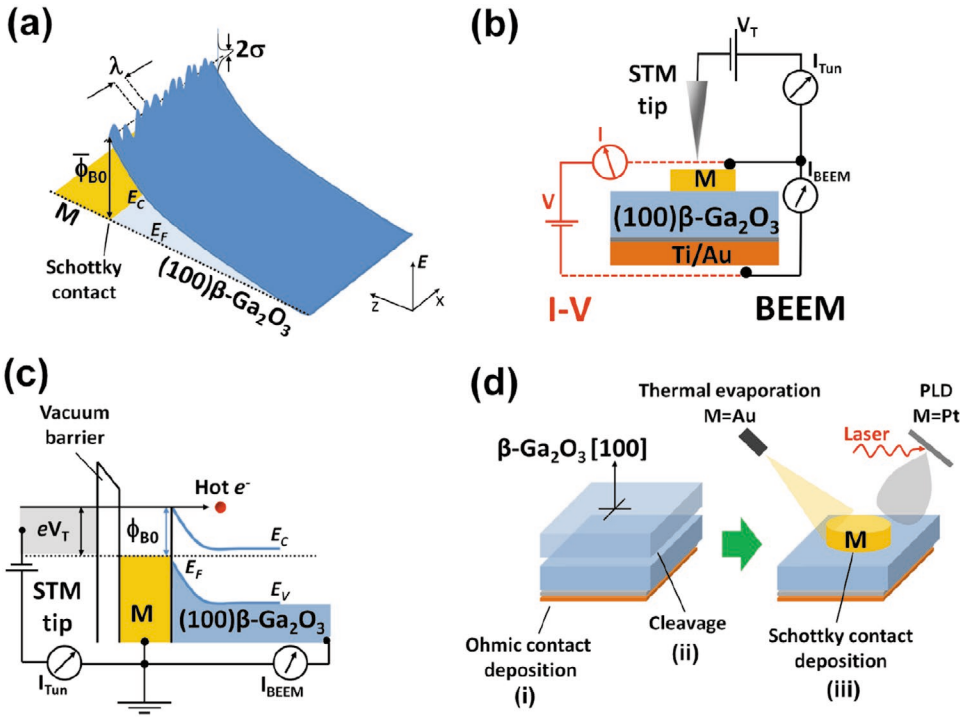

Figure 1. a) Spatially inhomogeneous potential landscape at an unbiased metal/(100)β-Ga_2O_3 interface, following a Gaussian distribution with mean value $\bar{\phi}_{B0}$, standard deviation σ, and characteristic length scale λ. b) Schematic diagram of the SBD with the experimental setup for *I–V* and BEEM measurements. c) Band diagram, with hot electron injection above the local SBH ϕ_{B0}. d) Fabrication steps of the SBDs.

interfacial oxygen vacancies V_O.[7] This description recalls the Schottky barrier formation mechanism on ZnO,[20] although firm experimental evidences are needed for β-Ga_2O_3.

The aforementioned complexity makes the metal/β-Ga_2O_3 interface naturally prone to spatial heterogeneity. In fact, there are growing evidences that interfacial transport is dominated by a patched interface with a laterally nonuniform SBH that leads to a range of non-ideal behaviors[9,21] and device-to-device variations.[10] It is common practice to quantify the degree of inhomogeneity indirectly, that is, via data modeling through the Werner and Guttler (WG) model.[22] This assumes dominant thermionic emission (TE) and parallel conduction through a continuum of independent diodes having a Gaussian-distributed local SBH (**Figure 1**a). Such an approach has the advantage that inhomogeneity is estimated from conventional macroscale transport studies. Accordingly, spatial fluctuations of SBH have been evaluated to be of ≈120–150 meV[9,11] for β-Ga_2O_3 SBDs that matches analogous estimates for other crystalline and amorphous wide-bandgap (WBG) semiconductors (e.g., GaN, ZnO, InGaZnO).[23] However, some assumptions of the WG model are not always satisfied, as other channels besides TE might contribute to transport, depending on the system details. Also, the characteristic length scale of spatial inhomogeneity λ remains unknown, whereas multiscale inhomogeneity related to multiple sources of interfacial disorder cannot be addressed. Paradigmatic to this purpose is the transition from single-threshold to double-threshold *I–V* characteristics, documented by Yao et al.[10] for β-Ga_2O_3 SBDs, as the size of the contact increases. According to Yao et al.,[10] this occurs because of the interplay of nanoscale inhomogeneity and interface defects located on the millimeter length scale, a situation that cannot be addressed by the WG model.

In this respect, proximal probe methods suitable to directly determine band bending in a spatially resolved way and as a function of the relevant controllable parameters (e.g., doping, temperature, environment) offer new opportunities to understand the true physical origin of the non-ideal behavior in order to reduce or eliminate it, and thus advance the current state of the art for the development of high-quality β-Ga_2O_3 rectifiers. Ballistic electron emission microscopy (BEEM) is a scanning tunneling microscopy (STM)-based technique that can directly measure the SBH at the metal/semiconductor interface with nanoscale accuracy. In BEEM, an STM tip at bias V_T injects ballistic electrons into a thin metal overlayer at a constant tunneling current I_{Tun} (Figure 1b). If the electrons kinetic energy $e|V_T|$ can overcome the buried energy barrier formed between the metal and the semiconductor, a current I_{BEEM} is transmitted across the sample and collected through the backside Ohmic contact.[24] The local SBH, ϕ_{B0}, is then defined by the onset of the collector current in I_{BEEM} versus V_T spectra (Figure 1c). Most of the BEEM studies have focused on SBDs involving non-oxidic semiconductors (e.g., Si, Ge, GaAs, SiC, GaN, ZnSe),[24,25] and only recently BEEM succeeded to probe devices based on the perovskite transition metal oxide $SrTiO_3$ (Nb-doped, *n*-type).[26–28] Hereafter, we demonstrate that BEEM can effectively investigate SBDs fabricated onto freshly cleaved (100)β-Ga_2O_3 single crystal substrates. Mechanical cleavage can in fact provide surfaces suitable for fundamental spectroscopic studies.[4,12,29] We explore Schottky interfaces prepared by two depositions methods, namely thermal evaporation and pulsed

laser deposition (PLD), the latter being largely exploited for the fabrication of β-Ga_2O_3 thin films and related heterojunctions.[30] Our study gives direct access to the nanoscale band bending and spatial inhomogeneity as function of temperature, vacuum exposure, and metallization protocols. Therefore, we provide a basis reference to benchmark the interfacial quality of β-Ga_2O_3 SBDs against state-of-the-art WBG semiconductor rectifiers, and to advance transport modeling in realistic contacts.[31] Additionally, we document a remarkable modulation of the nanoscale SBH (≈0.2 eV) upon device exposure to an oxygen-rich atmosphere.

2. Results and Discussion

2.1. Macroscopic Transport

Figure 1d presents a schematic illustration of the fabrication process of β-Ga_2O_3 SBDs. The details can be found in Section 4, but in short, the fabrication starts from i) deposition of the Ohmic contact on the backside of a single crystal (100) β-Ga_2O_3, then proceeds respectively with ii) cleavage in air of the single crystal, and iii) deposition of the Schottky metal. **Figure 2**a,b depicts *I–V* characteristics acquired in ultra-high vacuum UHV for a representative Au/(100)β-Ga_2O_3 junction. They were measured after exposure of the device to UHV for a few days (time in vacuum $t_{UHV} \approx 150$ h measured after grounding the Au pad by silver paste in air). Indeed, such a long t_{UHV} was necessary to achieve stationary rectifying properties (see Section 2.3 for the evolution of interfacial transport in vacuum for shorter t_{UHV}). All curves show rectification with polarity consistent with the β-Ga_2O_3 carrier type. At RT (Figure 2a), the current in the positive bias region increases exponentially from $\approx 3 \times 10^{-11}$ up to $\approx 1 \times 10^{-4}$ A, whereas the reverse bias leak current stays below 2×10^{-11} A. An excellent rectification ratio of $\approx 3 \times 10^7$ can be estimated at ± 1.0 V. As the characteristic is visualized for both sweep directions (see black arrows), hysteresis is also visible under reverse bias and for a low forward bias (below ≈0.5 V) and corresponds to the splitting of the current zero-crossings. This behavior, already documented for diodes based on β-Ga_2O_3 single crystals and thin film,[11,15] can be explained in terms of the charging and discharging current of an additional parallel capacitance caused by surface, interface, or deep-subsurface defects.[15] For forward voltages above ≈0.5 V, a nearly ideal mono-exponential slope is observable independent of the sweep direction, whereas above ≈0.9 V, both the semiconductor transport properties and the series resistance dominate. Similar features also occurred at temperatures below RT (Figure 2b).

To analyze the *I–V* curves, we assumed TE as the dominant transport mechanism[12,13] and we interpolated the exponential growth of the forward bias region with the TE theory, $J = A^* T^2 \exp(-\phi_B^{eff}/k_B T) \exp(qV/nk_B T)$, where J is the current density, and both the ideality factor n and the effective SBH ϕ_B^{eff} are fitting parameters. A theoretical Richardson constant A^* = 41.1 A cm^{-2} K^{-2} ($m^* = 0.342 m_0$) was used.[9] At RT, we obtained $\phi_B^{eff} = 1.32$ eV and n = 1.16. The former is in the middle range of values previously reported for Au/β-Ga_2O_3 single crystal interfaces (1.02–1.71 eV).[12–14] Idealities $n > 1$ have been often reported for metal/β-Ga_2O_3 single crystal diodes ($n \approx 1.09 - 1.2$) and suggest the existence of spatial inhomogeneity.[9,11,15] This assumption is confirmed by the TE analysis of *I–V–T* characteristics.

Figure 2b,c shows that the junction response strongly depends on temperature T, as a simultaneous lowering of ϕ_B^{eff} and increase of n take place on decreasing T. Such a trend is commonly assumed as a signature for the existence of a distribution of barriers.[22] In fact, at low temperatures, electrons can only surmount the lower barriers, and transport is dominated by the current flowing through the patches with lower SBH. In the framework of the WG potential fluctuations model assuming Gaussian variations of the local barrier height (Figure 1a),[22] the mean barrier $\overline{\phi_B^{eff}}$ and the standard deviation σ_{I-V} of the distribution are obtained by linear regression of the experimental $\overline{\phi_B^{eff}}(T)$ *vs* 1/T plot with the theoretical relationship $\phi_B^{eff}(T) = \overline{\phi_B^{eff}} - q\sigma_{I-V}^2/2k_B T$. Figure 2d shows that experimental data can be satisfyingly fitted with a straight line over the temperature range 80 K ≤ T ≤ 296 K, with best-fit parameters $\overline{\phi_B^{eff}} \cong 1.54$ eV and $\sigma_{I-V} \cong 103$ meV. The former is in the upper range of the effective barriers reported in literature for thermally-evaporated Au/(100)β − Ga_2O_3 and sputtered Au/($\bar{2}$01)β−Ga_2O_3 contacts (1.07–1.27 eV).[7,12] Also, σ_{I-V} is close to the estimates from the *I–V* analysis of Cu/($\bar{2}$01)β−Ga_2O_3 and Pt/(100)β-Ga_2O_3 SBDs under comparable doping conditions (126–130 meV).[9,11] As for other oxide semiconductors (e.g., $SrTiO_3$, ZnO), σ_{I-V} might be ascribed to heterogeneity of an unintentional defective "interfacial layer" created in the near-interface region either during oxide surface preparation or metal deposition. We underline that the WG model does not account for deviations of transport from TE neither any evolution of the interface energetics with T. Hence, its full applicability remains questionable (see Section S1, Supporting Information).

Contrary to the Au/(100)β-Ga_2O_3 case, the macroscopic response of a representative Pt/(100)β-Ga_2O_3 diode prepared by PLD resulted in a double-threshold *I–V* curve ($t_{UHV} \approx 215$ h; see Section S1, Supporting Information). Such behavior has been reported by many authors[7,8,10,16] and is attributed to interfacial patch effects roughly modeled as two independent diodes in parallel: one diode with higher SBH ϕ_{BH}^{eff} and the other one with lower barrier ϕ_{BL}^{eff}. From interpolation with TE theory, we obtained $\phi_{BL}^{eff} = 0.84$ eV and $\phi_{BH}^{eff} = 0.90$ eV at RT. Both SBHs are in the lower range of values reported for interfaces prepared by electron-gun evaporation, sputtering or thermal evaporation of Pt (0.71–1.5 eV).[4] The manifestation of the non-ideality hampers applying the WG model, therefore estimation of interfacial inhomogeneity from *I–V* curves was not feasible for the Pt SBD. We next show that BEEM can circumvent such a limitation and achieve a consistent description of the nanometer-scale interfacial patches for both evaporated and PLD-grown SBDs.

2.2. Nanoscale Band Bending and Interfacial Inhomogeneity

In **Figure 3**a,b, we show topography and BEEM maps simultaneously acquired at RT over a representative region of the evaporated Au electrode (same device of Figure 2). The topography is typical of the 3D (Volmer–Weber) growth of ultrathin

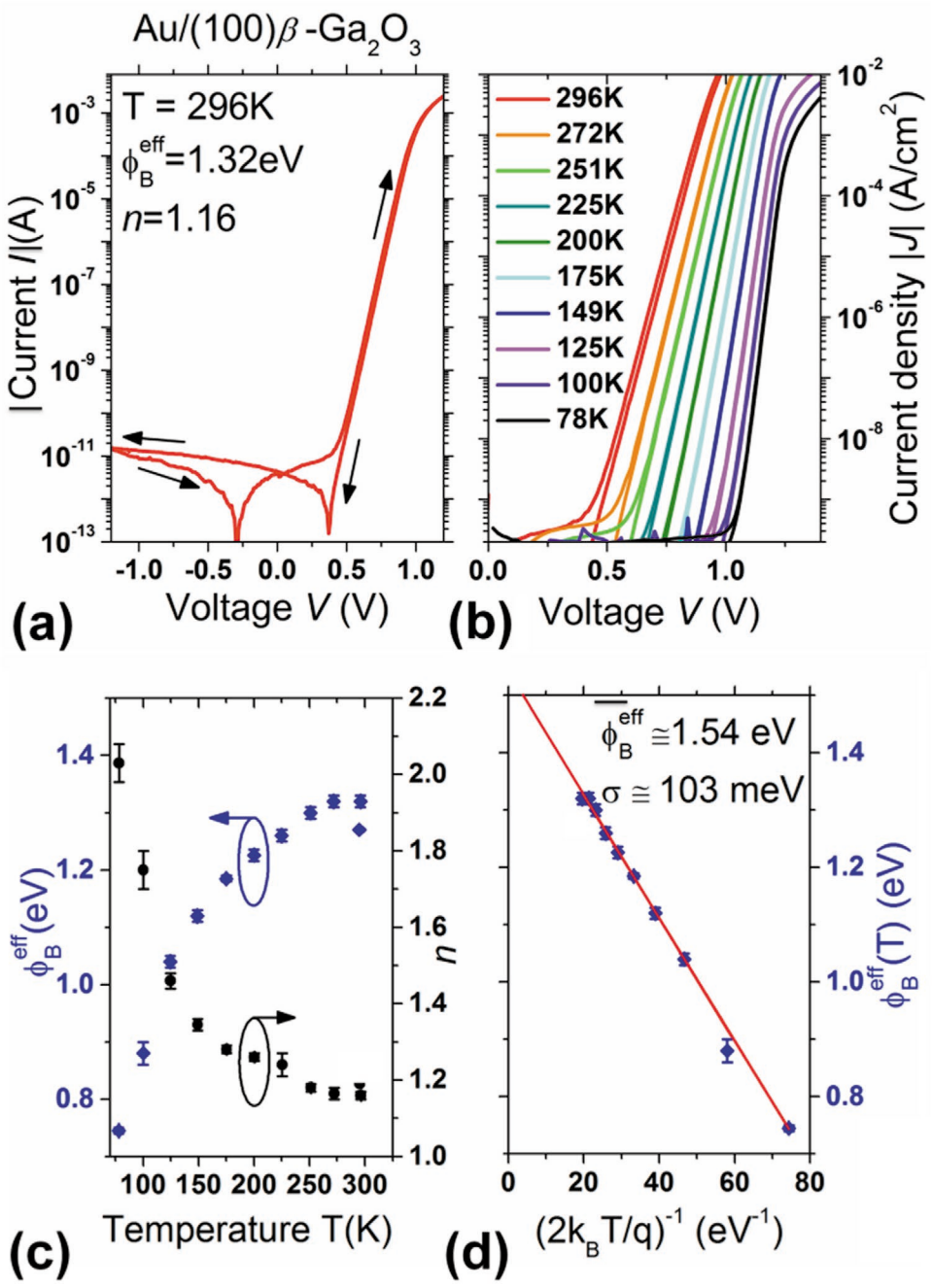

Figure 2. a) RT *I–V* curve of a thermally evaporated Au/(100)β-Ga_2O_3 SBD measured in UHV ($t_{UHV} \approx 150$ h). Sweep directions are indicated by black arrows. b) Temperature-dependent *J–V* curves (forward branch) for the same device in (a). c) The temperature-*dependence* of the effective barrier height ϕ_B^{eff} and ideality factor *n* indicates a patched interface with a distribution of barriers. d) Plot of $\phi_B^{eff}(T)$ versus $1/T$. Interpolation (red curve) is done with the WG Gaussian fluctuation model (see text).

metal films on dielectric substrates,[32] and consists of a percolating network of islands separated by irregular channels. The discontinuous morphology is likely favored by the moderate radiative heating (≈60 °C) of the β-Ga_2O_3 substrate during deposition, that enhances (liquid-like) metal clustering.[33] The surface heights' range (≈10 nm) fits the Au nominal thickness, hence the channels likely yield to the bare substrate or to an atomically thin wetting layer. The BEEM map (Figure 3b) reveals hot electron injection across the whole interface, with spatial variations of ballistic current I_{BEEM} localized at specific spots with very intense contrast (≈50–100%). By overlapping the maps of BEEM current and STM topography (Figure 3c), we did not find any trivial correlation between the two signals, as I_{BEEM} does not change systematically with the local surface slope or the thickness of the Au film,[28] and neighbor islands often present different BEEM contrast. Hence, BEEM map

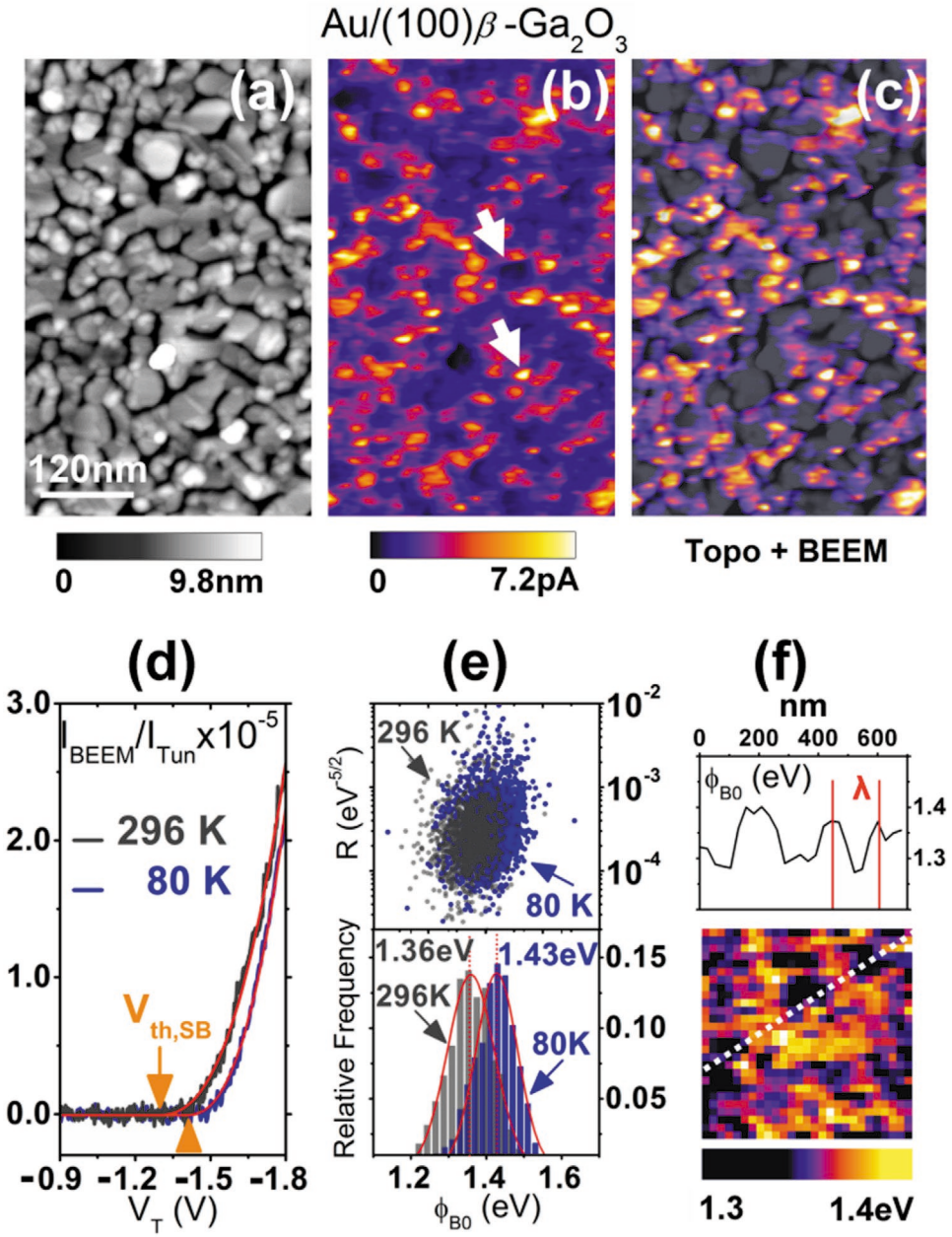

Figure 3. a) STM topography and b) BEEM map acquired simultaneously over a representative Au region of the Au/(100)β-Ga_2O_3 junction (I_T = 36 nA, V_T = –1.95 V, T = 296 K). The arrows highlight two localized spots with high BEEM contrast. c) Overlapped "Topo + BEEM" map does not reveal any systematic correlation of BEEM contrast with the Au morphology. d) Representative BEEM spectra. Red lines are fits with the LP model. e) Dual parameter (ϕ_{B0}, R) distributions (top) and ϕ_{B0} histograms. Red lines are Gaussian fits. f) Spatially resolved map of ϕ_{B0}. Along the dash line, ϕ_{B0} fluctuates over a length scale λ as large as ≈200 nm.

reflects multiple contributions, from the polycrystalline nature of the Au film and from lateral inhomogeneity in the electronic, chemical, or spatial structure of the Au/(100)β-Ga_2O_3 interface.

To gain deeper insight, BEEM spectroscopy was carried out at variable temperatures. In Figure 3d, we compare representative spectra acquired, respectively, at 296 and 80 K. Each spectrum shows a monotonic behavior, with the threshold $V_{th,SB}$ corresponding to the local value of the SBH, $\phi_{B0} = e|V_{th,SB}|$. On reducing T, ϕ_{B0} increases from ≈1.29 to ≈1.40 eV, whereas the hot electron injection efficiency I_{BEEM}/I_{Tun} stays in the range $\approx 2 - 3 \times 10^{-5}$ at $V_T = -1.8$ V.

We further explored this phenomenology quantitatively, by fitting an ensemble of about 3800 spectra with the Ludeke and Prietsch (LP) model $I_{BEEM}/I_{Tun} = R(V_T - V_{th,SB})^{5/2}$ (fitting range -0.4 V $< V_T < -1.9$ V) to estimate $\phi_{B0} = e|V_{th,SB}|$ and the transmission attenuation factor R.[24] The related dual parameters' (ϕ_{B0}, R) distributions and the ϕ_{B0} histograms are reported in Figure 3e. Local variations in the intensity and onsets of BEEM spectra caused a remarkable spreading of

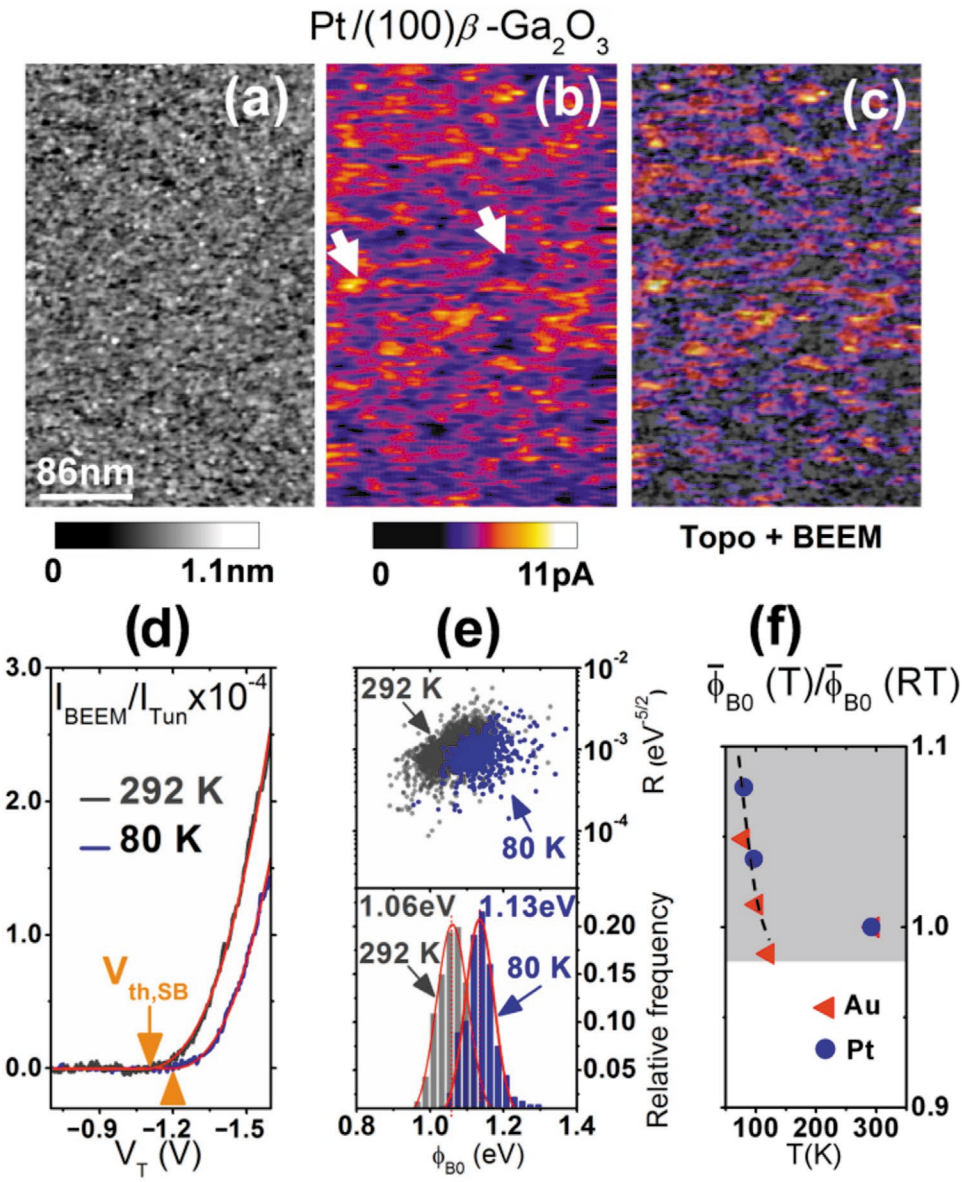

Figure 4. a) STM topography and b) BEEM map for a representative Pt region of the Pt/(100)β-Ga_2O_3 junction (I_T = 25 nA, V_T = –1.60 V, T = 292 K). Arrows highlight two localized spots with high BEEM contrast. c) The overlapped "Topo + BEEM" map does not reveal any systematic correlation of BEEM contrast with the Pt morphology. d) Representative BEEM spectra. Red lines are fits with the LP model. e) Dual parameter (ϕ_{B0}, R) distributions (top) and ϕ_{B0} histograms. Red lines are Gaussian fits. f) Temperature dependence of the spatially averaged SBH, $\overline{\phi_{B0}}(RT)$, for Au and Pt SBDs. Dash line is a guide to eye. Note that $\overline{\phi_{B0}}(T)$ is normalized to its RT value, $\overline{\phi_{B0}}(RT)$.

the ϕ_{B0} and R parameters. In particular, the barrier spread at 296 K is from ≈1.2 up to ≈1.5 eV. The Gaussian histogram of SBH is centered at the mean value $\overline{\phi_{B0}} = 1.36$ eV, very close to $\phi_B^{eff}(296\text{ K}) = 1.32$ eV estimated by I–V analysis. The barrier inhomogeneity at the Au/(100)β-Ga_2O_3 is $\sigma_{Au}(296\text{ K}) \approx 63$ meV (standard deviation). According to Figure 3e, at T = 80 K the distribution (ϕ_{B0}, R) shifts laterally, corresponding to an overall increase of the local ϕ_{B0} values. The SBH histogram is centered at $\overline{\phi_{B0}} = 1.43$ eV and $\sigma_{Au}(80\text{ K}) \approx 56$ meV. Hence, $\overline{\phi_{B0}}$ decreases by ≈70 meV from 80 to 296 K.

Spatially resolved maps of the local barrier height ϕ_{B0} revealed heterogeneity of the interface over a length scale of tens of nanometers (see Sections S2.1 and S2.2, Supporting Information). In particular, large-sized patches of uniform ϕ_{B0} with size λ up to ≈200 nm were very common, as shown in Figure 3f.

Figure 4 resumes BEEM data for the Pt/(100)β-Ga_2O_3 junction. Qualitatively, BEEM map contrast and BEEM spectroscopy share strong similarities with the Au interface (Figure 4a–d), albeit STM topography now revealing a compact nanocrystalline Pt film, formed by the coalescence of grains of a few nanometers in size. The ϕ_{B0} histograms, obtained by LP fitting of an ensemble of 3400 individual spectra, indicate a mean value $\overline{\phi_{B0}} = 1.06$ eV at 292 K (Figure 4e), which is higher than both $\phi_{BH}^{eff}(292\text{ K}) = 0.90$ eV and $\phi_{BL}^{eff}(292\text{ K}) = 0.84$ eV estimated from I–V analysis. The barrier inhomogeneity amounts

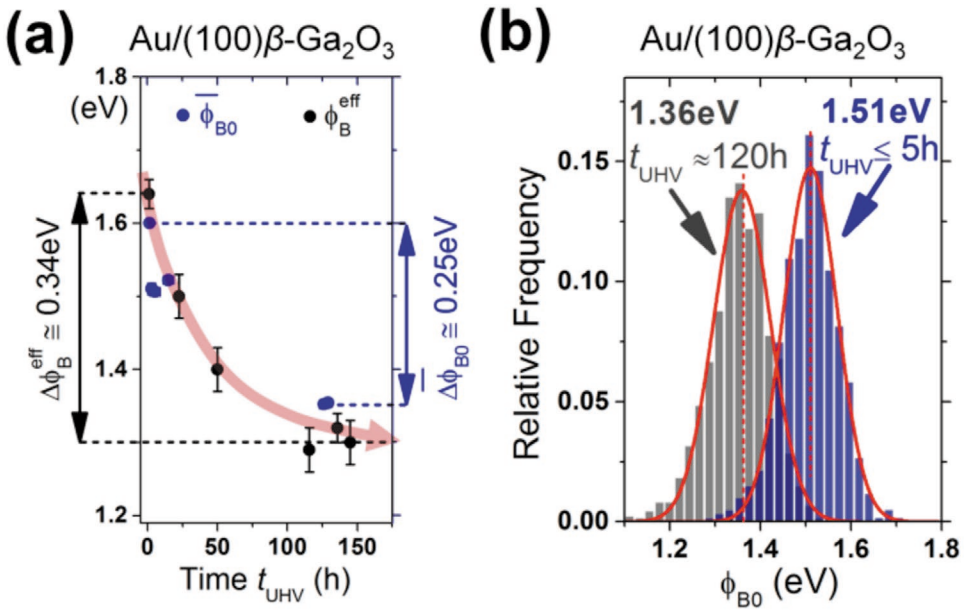

Figure 5. a) Modulation of the SBH at the Au/(100)β-Ga_2O_3 interface as a function of the time of permanence in UHV, t_{UHV} (time zero corresponds to the insertion time of the device in UHV from air). Red arrow is a guide to eyes. b) Evolution of the nanoscale ϕ_{B0} histograms with t_{UHV}, for the same device studied in (a). Solid curves are Gaussian fits.

to σ_{Pt} (292 K) ≈ 43 meV. At the lower temperature T = 80 K, $\overline{\phi_{B0}} = 1.13$ eV and σ_{Pt} (80 K) ≈ 39 meV. Also, spatially resolved maps of the local barrier height ϕ_{B0} revealed features in line with those highlighted in Figure 3f for the Au pad, with $\lambda \sim 20 - 200$ nm (see Section S2.2, Supporting Information).

From BEEM spectroscopy, one concludes that the Au/ and Pt/(100)β-Ga_2O_3 interfaces share a relevant similarity at the nanoscale. First, i) all BEEM spectra are satisfyingly fitted by the LP model with one characteristic threshold $V_{th,SB}$ (see Section S2.3, Supporting Information). Second, ii) the inhomogeneous SBH varies on a length scale λ of tens of nanometers, with mean values $\overline{\phi_{B0}} = 1.06$ eV (Pt) – 1.36 eV (Au) and standard deviations as small as σ = 43 meV(Pt) – 63 meV(Au) at RT. Third, iii) by changing the working temperature T, $\overline{\phi_{B0}}$ changes by ≈70 meV regardless of the Schottky metal pad. Concerning (i), the energy band structure of β-Ga_2O_3 shows a direct conduction band minimum at the center (Γ) of the Brillouin zone, whereas other conduction band minima are predicted to be at least 2 eV higher. The single threshold of the spectra thus originates—according to the general BEEM theory[24,25]—from hot electrons injection into the conduction band minimum at the center zone Γ. Regarding (ii), $\overline{\phi_{B0}}$ values agree with predictions for the transition level of the doubly ionized fourfold-coordinated oxygen vacancies V_O^{2+}(III) (approx. E_C – 1.12 eV from Varley et al.,[34] approx. E_C – 1.2 eV from Dong et al.[35]), thus supporting arguments that the SBH at different β-Ga_2O_3 surface terminations is controlled by FL pinning, generated by native defects or interface states close to $V_O(2+/0)$.[7] Regarding (iii), **Figure 5**f shows that the SBH sharply increases below 150 K. Note that the slope of –3 meV K^{-1} is by a factor 10 higher than that previously reported by Huber et al.[21] and by He et al.[17] from macroscale I–V measurements conducted above RT. Possible explanations to such a trend might rely on the temperature dependences of the (100)β-Ga_2O_3 bandgap (≈0.1 eV in the range 20 K–RT) and of the static dielectric constant $\varepsilon_r(T)$,[3,4,27] or even on surface charge trapping/detrapping effects. Note that such a pronounced temperature dependence is not accounted for by the WG model. We also underline that the similarity between Au/ and Pt/(100)β-Ga_2O_3 SBDs at the nanoscale strikingly contrasts with their dissimilar behavior at the macroscale (see Section S2.4, Supporting Information).

Aside from previous discussion, the BEEM capability to probe nanoscale inhomogeneity enables to directly compare (100)β-Ga_2O_3 SBDs with other technologically relevant junctions. Since σ is an effective quantity, summing up heterogeneity contributions from native substrates and from fabrication protocols, it can be exploited as a figure-of-merit to settle a nanoscale benchmark of WBG semiconductor rectifiers. As shown in **Table 1**—where state-of-the-art SBDs are arranged (from top to bottom) in terms of increasing σ—the studied (100)β-Ga_2O_3 SBDs display smaller inhomogeneity than Nb:$SrTiO_3$-based devices; they are comparable to GaN and ZeSe diodes and turn out to be not far from the 4H-SiC and InGaP ones. This comparison indicates that contacts to air-cleaved (100)β-Ga_2O_3 single crystals do have an interfacial quality fitting the more established standards. Also, this analysis provides great promise for SBDs prepared onto high-quality β-Ga_2O_3 epilayers, which characterization is ongoing[36] and which fabrication was shown to relieve some of the sources of interfacial disorder induced by the physical separation in cleaved bulk crystals (e.g., dangling bonds, multiple terminations, point defects).[4]

2.3. Modulation of SBH by Ambient Atmosphere

As mentioned above, the as-fabricated SBDs were briefly exposed to laboratory air (≈15 min.) for Au and Pt grounding

Table 1. Benchmark of state-of-the-art SBDs based on WBG semiconductors (doping *n*-type in all cases).

Semiconductor		Metal	Deposition	$\overline{\phi_{Bo}}$ [eV]	σ [meV] ↑	N_D [cm^{-3}]	T [K]	Ref.
GaP	*epi (100)*	Au	*e-g*	1.33	19	1.1×10^{17}	RT	[53]
$In_{0.1}Ga_{0.9}P$	*epi (100)*	Au	*e-g*	1.46	24	7×10^{16}	RT	[53]
$In_{0.49}Ga_{0.51}P$	*epi (100)*	Au	*e-g*	1.14	30	1.6×10^{16}	RT	[53]
6H-SiC	*epi (0001)*	Pd/Pt	*e-g*	1.27/1.34	<30	3×10^{16}	RT	[54]
4H-SiC	*epi (0001)*	Pd/Pt	*e-g*	1.54/1.58	<40	5×10^{18}	RT	[54]
ZnSe	*epi (100)*	Au	*thermal*	1.38–1.65	20–50	1×10^{16} to 5×10^{18}	RT	[53,55]
β-Ga_2O_3	*SC (100)*	Pt	*PLD*	1.13–1.06	39–43	6×10^{17}	80–RT	This work
β-Ga_2O_3	*SC (100)*	Au	*thermal*	1.43–1.36	56–63	6×10^{17}	80–RT	This work
GaN	*epi (100)*	Au	*thermal*	0.70–1.04	70–90	5×10^{16}	RT	[56]
Nb:$SrTiO_3$	*SC (100)*	LSMO	*PLD*	0.83–0.87	50–100	8×10^{18}	120–RT	[26]
Nb:$SrTiO_3$	*SC (100)*	Au	*thermal*	1.32	85–117	1×10^{18} to 1.7×10^{20}	80–RT	[27,28]

Both SBH $\overline{\phi_{Bo}}$ and spatial inhomogeneity σ are estimated by BEEM in UHV.
epi, epilayer; *SC*, single crystal; *e-g*, electron-gun evaporation; *thermal*, thermal evaporation; *PLD*, pulsed laser deposition.

(i.e., contact formation with silver paste), before being inserted into UHV. After insertion into vacuum, SBDs showed a slow evolution of the RT interfacial transport within the first ≈100 h, after which they achieved the rectifying properties discussed above (Figures 2 to 4). In Figure 5a, we show the typical response of the Au/(100)β-Ga_2O_3 interface in vacuum. The *I*–*V* characteristics indicate a reduction $\Delta\phi_B^{eff} \cong 0.34$ eV over a total exposure time $t_{UHV} \approx 110$ h. Consistently, BEEM data (from an ensemble of about 2300 spectra) attest a decrease $\Delta\overline{\phi}_{B0} \approx 0.25$ eV on going from exposure time $t_{UHV} = 1$ h ($\overline{\phi}_{B0} = 1.60$ eV) to $t_{UHV} = 120$ h ($\overline{\phi}_{B0} = 1.35$ eV). Inspection of the ϕ_{B0} histograms at different stages of the interfacial evolution (Figure 5b) shows that vacuum exposure mainly causes a reduction of $\overline{\phi_{B0}}$, whereas σ_{Au} does not significantly vary with t_{UHV} ($\sigma_{Au} \approx$ 59 – 62 meV) and remains in the range of values discussed before. Hence, inhomogeneity σ_{Au} estimated by BEEM depicts a robust property of the Au/(100)β-Ga_2O_3 interface not affected by t_{UHV}. To better illustrate the vacuum sensitivity for the Au/(100)β-Ga_2O_3 interface, two important facts are to be mentioned. First, the SBH evolution of Figure 5a could be reversed by exposure of the SBD to laboratory air. In fact, air exposure for ≈30–60 min was sufficient to recover the initial SBH values $\phi_B^{eff} \sim \overline{\phi}_{B0} \sim 1.60$ eV, which indicates a reversible interaction of the interface with ambient air at RT. Second, sensitivity to UHV was greatly reduced for junctions exposed to dry air (in a dessicator) for several months. In such case, the effective SBH achieved a permanent value as high as $\phi_B^{eff,AIR} = 1.82$ eV and rectification improved, as attested by the decrease of *n* from 1.16 (Section 2.1.) to 1.10 (**Figure 6**a).

For the Pt/(100)β-Ga_2O_3 interface, BEEM data attested a decrease $\Delta\overline{\phi}_{B0} \approx 0.24$ eV almost coincident to that measured for the Au/(100)β-Ga_2O_3 interface over a similar t_{UHV} range. However, a reduction of interfacial inhomogeneity σ_{Pt} also took place. Moreover, the variation of ϕ_{BH}^{eff} amounted only to $\Delta\phi_B^{eff} \cong 0.06$ eV. Hence, vacuum evolution was more complex than that of the Au/(100)β-Ga_2O_3 counterpart (see Section S3.1, Supporting Information).

2.4. Description of the Metal/β-Ga_2O_3 Interface

Besides the case of β-Ga_2O_3 SBDs, the RT reduction of the SBH in vacuum (upon air exposure) has been documented for Au/Nb:$SrTiO_3$[19] and Pt/Nb:$SrTiO_3$[37] SBDs. There is consensus that this phenomenology reflects interaction with the environment through (thermally activated) oxygen-exchange reactions at the Schottky interface. Two different scenarios might be invoked. The first one involves surface/interface adsorption of ionic species (Figure 6b) and relies on the general ionosorption theory, which is the paradigm of oxygen-sensing for several *n*-type semiconducting metal oxides (e.g., SnO_2, TiO_2, ZnO).[19,38] The model assumes that atmospheric oxygen adsorbs on the semiconductor surface as molecular and atomic ions (e.g., O_2^-) that trap electrons from the conduction band. Such process results in the accumulation of negative charge at the oxide surface and the formation of an electron-depleted layer in air or in oxygen-rich atmosphere, with a subsequent upward surface band bending and a decrease of the surface conductance. The opposite occurs in vacuum, due to oxygen desorption from the oxide surface. Accordingly, the decrease of the SBH in vacuum for metal/(100)β-Ga_2O_3 interfaces ($\Delta\overline{\phi}_{B0} \approx 0.24 - 0.25$ eV, $\Delta\phi_B^{eff} \approx 0.06 - 0.34$ eV) might reflect desorption of the ionosorbed oxygen and depopulation of the negative charges accumulated at the β-Ga_2O_3 surface layer while handling substrates in air (after cleavage and/or for contact formation). Since in *n*-type metal oxides the reactive sites for oxygen adsorption are surface point defects, the sensitivity to ambient oxygen should depend on the degree of oxidation and stoichiometry of the interface. In fact, a defect-initiated adsorption mechanism was invoked in literature to account for the RT gas sensing capability of β-Ga_2O_3 nanowires.[39]

The second scenario we propose involves redox surface chemistry and ascribes a relevant role to interface oxygen vacancies V_O and oxygen ions motion (Figure 6c). The weak dependence of the SBH on the metal work function ϕ_M, documented across a range of metals (i.e., Pd, Ni, Pt, Au) deposited

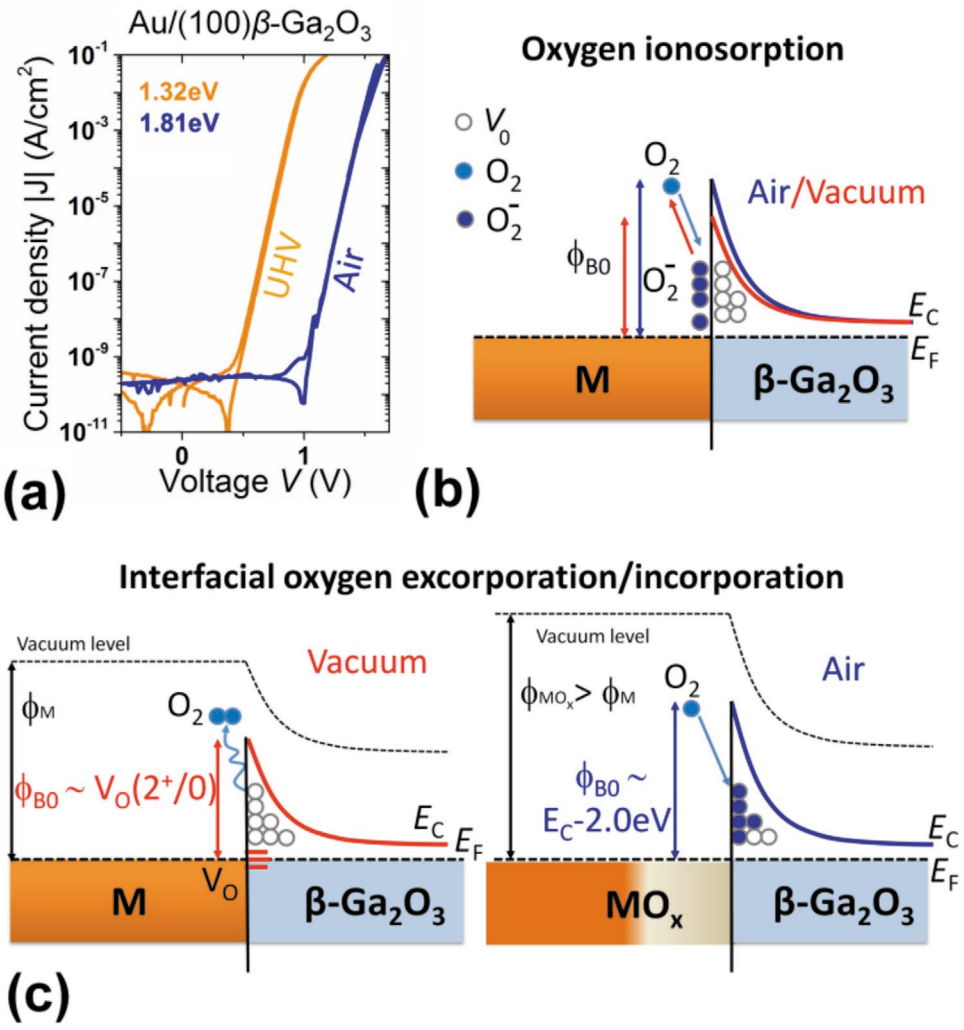

Figure 6. a) Response of the same Au/(100)β-Ga_2O_3 device to ambient atmosphere. Macroscale SBH values are in the inset. b,c) Models of oxygen-exchange reactions at the metal/β-Ga_2O_3 interface (see text).

on single crystal β-Ga_2O_3 with (010) and $(\bar{2}01)$ surface terminations, suggests that FL pinning by crystallographic point defects[40] might partially or fully dominate the Schottky barrier formation.[7] In particular, FL pinning by V_O was previously proposed[7] to explain the narrow range of SBHs close to the $V_O(2+/0)$ transition level. In fact, for β-Ga_2O_3, there are three inequivalent oxygen sites: threefold coordinated O(I) and O(II) and fourfold coordinated O(III). According to calculations and experiments,[34,35] the smallest transition level regards O(III) and amounts to ≈1.12–1.2 eV below E_C. Hence, it is likely that the doubly ionized fourfold-coordinated vacancy defects V_O^{2+}(III) have a prominent role in the FL pinning at the interface. In this respect, we speculate that the decrease of the SBH in vacuum might reflect the slow increase in time of the V_O^{2+}(III) density due to oxygen excorporation from the near interface layer and subsequent FL pinning to the V_O(III) (2 + /0) transition level. According to Hou et al.,[7] this gives an SBH ≈1.1–1.4 eV, that readily matches our BEEM results ($\overline{\phi_{B0}}$ = 1.06 eV (Pt) – 1.36 eV (Au)). On the other hand, the increase of the SBH after ≈30–60 min of exposure to air might originate from some healing of interfacial V_O^{2+}(III) defects that rises interfacial band bending by $\Delta\overline{\phi}_{B0} \approx 0.24 - 0.25$ eV. As observed by Hou et al.,[7] this latter process might possibly result—in the long term—in unpinning of the FL from V_O(III) (2 + /0) level to the estimated E_C – 2.0 eV location of the charge neutrality level φ_{CNL}, or to other deep-level defects at E_C – 2.0 eV.[40] We underline that the assumption of an effective modulation of V_O content during vacuum/air exposure is qualitatively in line with spectroscopic results for other *n*-type oxide semiconductors (e.g., Nb:$SrTiO_3$[41]), but it does not necessarily reflect direct V_O annihilation/creation by ambient O_2 as a more complex defects chemistry might be involved depending on the specific surface chemistry equilibria of (100)β-Ga_2O_3.[42] This second scenario seems particularly plausible, in view of the excellent agreement between our data for Au/(100)β-Ga_2O_3 interface and results for in situ oxidized Au/$(\bar{2}01)\beta$-Ga_2O_3.[7] In fact $\overline{\phi_B^{eff}} = 1.20 \pm 0.01$ eV for Au/$(\bar{2}01)\beta$-Ga_2O_3 SBDs prepared in a low-oxygen atmosphere, which increases to $\overline{\phi_B^{eff}} = 1.81 \pm 0.09$ eV by in situ oxidation during Au deposition.[7] This gives an overall variation $\Delta\phi_{ox}$ = 0.54 eV. Remarkably, $\Delta\phi_{ox}$

matches the quantity $(\phi_B^{eff,AIR} - \phi_B^{eff,UHV})_{Au} = 0.48$ eV we measured for evaporated Au SBD stored in air/UHV, respectively, which greatly supports previous arguments. Measurements by Kelvin probe force microscopy on β-Ga_2O_3 thin films further confirm that point defects can modulate the work function of β-Ga_2O_3 by as much as ≈0.4 eV.[43] Following this picture, the metal/β-Ga_2O_3 interface appears dominated by an ubiquitous inhomogeneous interfacial layer that assists interfacial oxygen incorporation (excorporation) in air (vacuum).

The two suggested scenarios are not mutually excluding, rather they might coexist and interact at various levels. Both assume that the ultrathin Schottky electrodes offer an easy-permeable non-blocking interface for free-gas exchange at the substrate surface and within the nearby oxide interfacial layer (see Section S3.2, Supporting Information). Further experimental studies, conducted in a controlled oxygen atmosphere and offering surface chemistry sensitivity (e.g., by ambient pressure x-ray photoelectron spectroscopy AP-XPS),[41] are necessary to sort out specific pathways for the modulation of the SBH by the ambient atmosphere, including subtle effects due to Schottky metal thickness, device biasing,[44] or humidity effects[45] assisted by the water splitting capacity of the Au/(100)β-Ga_2O_3 interface.[46] Given previous discussion, we can finally attempt an evaluation of the origin of interfacial inhomogeneity measured by BEEM. General predictions from "donor-type" deep levels model[31] indicate that the SBH is sensitive to the concentration and position of charged defects and dopants within the oxide semiconductor near-interface region. Hence, sizable fluctuations of the SBH are expected for β-Ga_2O_3 due to V_O defects, for example, doubly positive V_O^{2+}(III) and V_O^{2+}(I). Fluctuations of SBH might also arise from local electron-affinity differences between the two energetically favored (non-polar) surface terminations called A and B, termination B being the dominant one for air-cleaved (100) substrates.[29]

Our findings are useful to engineer and model β-Ga_2O_3 rectifiers based on single crystal wafers[4,6,7] and exfoliated nanolayers,[47,48] for optoelectronics and gas-sensing applications in the low working temperature area. Knowledge of interfacial inhomogeneity σ and temperature-dependent $\overline{\phi_{B0}}(T)$ can advance transport modeling[31] of miniaturized contacts, in the effort to mimic the sophisticated design nowadays applied to SiC and GaN counterparts.[4] Furthermore, this study provides a solid ground to the "regime of random statistical fluctuations"[49] that is expected to dominate transport in ultra-scaled β-Ga_2O_3 SBDs, as they approach the critical size of the potential fluctuations $\lambda \approx 20 - 200$ nm. From a different perspective, the relative ease of modulation of the SBH by exposure to ambient gases—here documented at RT—adds significant knowledge to the growing body of literature about β-Ga_2O_3 surface effects,[50] sensitivity to environment being a key issue for the effective exploitation of β-Ga_2O_3.

3. Conclusion

In summary, we have presented a comprehensive characterization of nanoscale band bending and interfacial inhomogeneity for prototypical β-Ga_2O_3 SBDs, fabricated by deposition respectively of Au and Pt onto air-cleaved (100) single crystals. We have shown that inhomogeneity σ achieves a minimum after a few days of permanence in vacuum, and amounts to 40(Pt)–60(Au) meV over length scales of tens of nanometers. Exploitation of σ as a figure-of-merit reveals that the prepared junctions are fully comparable to state-of-the-art contacts to ZnSe and GaN epilayers, and are not far from 4H-SiC and InGaP Schottky contacts. We have also attested that such interfaces are sensitive to ambient atmosphere, with a modulation of the nanoscale SBH of ≈0.2 eV upon RT exposure to laboratory air. Besides a conventional rationalization of junction behavior via the oxygen ionosorption theory, we propose that environmental oxygen affects the content of fourfold-coordinated oxygen vacancies V_O(III) through thermally activated oxygen exchange reactions taking place within a defective (inhomogeneous) interfacial layer. Sensitivity to ambient gases could be limited by a number of methods to achieve stable operation (e.g., by use of thicker metal pads, by β-Ga_2O_3 surface passivation, or by device encapsulation); nonetheless, such feature marks the possibility to engineer β-Ga_2O_3 SBDs as gas-sensing devices operating nearby RT. The experimental approach described here can be extended to interfaces involving different surface terminations ($(\bar{2}01)$, (010)) and fabrication protocols. Hence, it provides a new opportunity to probe the full potential of β-Ga_2O_3 SBDs down to the nanoscale.

4. Experimental Section

Fabrication of Metal/(100) β-Ga_2O_3 SBDs: The radio-frequency heating edge-defined film-fed growth technique was used to produce unintentionally doped *n*-type β-Ga_2O_3 bulk single crystal substrates (net donor concentration ≈6×10^{17} cm^{-3}). The fabrication of SBDs started with the Ohmic contact formation. The rear side of each single crystal substrate was treated with an oxygen plasma, and two sequential layers of Ti (10 nm) and Au (240 nm) were deposited on it by sputtering to form the Ohmic cathode.[9] On the front side, the Schottky contacts were fabricated on the cleavage plane (100), freshly cleaved under ambient conditions[12,29] (crystal thickness after cleavage 50–140 µm). Circular contacts were prepared by metallization through a shadow mask (area 2.3 ± 0.1 mm^2), respectively, via thermal evaporation from a tungsten coil for Au (vacuum pressure <10^{-7} torr, deposition rate ≈1.5 nm min^{-1}, nominal thickness 10 nm) or by PLD for Pt (pressure 3×10^{-7} mbar, deposition rate ~0.5 nm min^{-1}, nominal thickness 8 nm).

Characterization of SBDs: After fabrication of the Schottky metal pads, the SBDs were exposed to ambient air for ≈15 minutes for contact formation.[19,28] After this step, SBDs were inserted into a UHV chamber (base pressure 5×10^{-10} mbar) for *I–V* and BEEM characterization. *I–V* curves were measured under dark with a Keithley 6430 sub-femtoamp sourcemeter, by sweeping the voltage with a delay time of 2 s per 10 mV steps. BEEM was performed under dark using a modified commercial STM, as explained elsewhere[28,51,52] (see also Section S2.1, Supporting Information). For time-lapse measurements addressing the temporal evolution of the Schottky interface under dark and at RT, *I–V* curves and BEEM spectroscopy were repeated at selected times starting from the insertion of the SBDs into the UHV chamber. Note that BEEM could be successfully performed only for SBDs fabricated onto freshly cleaved (100)β-Ga_2O_3, as I_{BEEM} was below our detection limit (≈15 fA) whenever we tested devices prepared without substrate cleavage (e.g., as in ref. [9]).

Supporting Information

Supporting Information is available from the Wiley Online Library or from the author.

Acknowledgements

The authors acknowledge the support by the National Natural Science Foundation of China (Grant Nos. 61925110, 5191101467 and 61821091), the National Key Research and Development Program of China (Grant No. 2018YFB0406504), the Key Research Program of Frontier Sciences of the Chinese Academy of Sciences (Grant No. QYZDB-SSW-JSC048), the Key Research and Development Program of Shandong Province (Grant No. 2018CXGC0410), the Young Scholars Program of Shandong University (Grant No. 2015WLJH36), the 111 Project 2.0 (Grant No. BP2018013), and the Italian MIUR through INFN-CNR national project (PREMIALE2012) "EOS Organic Electronics for Innovative Research Instrumentation. The device fabrication was partially carried out at the University of Science and Technology of China Center for Micro and Nanoscale Research and Fabrication. The authors would also like to thank the Information Science Laboratory of University of Science and Technology of China for its software and hardware services.

Conflict of Interest

The authors declare no conflict of interest.

Keywords

ballistic electron emission microscopy, gallium oxide, oxide semiconductors, oxygen vacancies, Schottky junctions

Received: October 17, 2019
Revised: December 2, 2019
Published online: January 22, 2020

[1] J. Y. Tsao, S. Chowdhury, M. A. Hollis, D. Jena, N. M. Johnson, K. A. Jones, R. J. Kaplar, S. Rajan, C. G. Van de Walle, E. Bellotti, C. L. Chua, R. Collazo, M. E. Coltrin, J. A. Cooper, K. R. Evans, S. Graham, T. A. Grotjohn, E. R. Heller, M. Higashiwaki, M. S. Islam, P. W. Juodawlkis, M. A. Khan, A. D. Koehler, J. H. Leach, U. K. Mishra, R. J. Nemanich, R. C. N. Pilawa-Podgurski, J. B. Shealy, Z. Sitar, M. J. Tadjer, et al., *Adv. Electron. Mater.* **2018**, *4*, 1600501.
[2] S. J. Pearton, J. Yang, P. H. Cary, F. Ren, J. Kim, M. J. Tadjer, M. A. Mastro, *Appl. Phys. Rev.* **2018**, *5*, 011301.
[3] H. von Wenckstern, *Adv. Electron. Mater.* **2017**, *3*, 1600350.
[4] S. J. Pearton, J. Yang, P. H. Cary, F. Ren, J. Kim, M. J. Tadjer, M. A. Mastro, *Appl. Phys. Rev.* **2018**, *5*, 011301.
[5] S. Müller, H. Von Wenckstern, F. Schmidt, D. Splith, H. Frenzel, M. Grundmann, *Semicond. Sci. Technol.* **2017**, *32*, 065013.
[6] C. Hou, R. M. Gazoni, R. J. Reeves, M. W. Allen, *IEEE Electron Device Lett.* **2019**, *40*, 337.
[7] C. Hou, R. M. Gazoni, R. J. Reeves, M. W. Allen, *Appl. Phys. Lett.* **2019**, *114*, 033502.
[8] R. Suzuki, S. Nakagomi, Y. Kokubun, N. Arai, S. Ohira, *Appl. Phys. Lett.* **2009**, *94*, 222102.
[9] G. Jian, Q. He, W. Mu, B. Fu, H. Dong, Y. Qin, Y. Zhang, H. Xue, S. Long, Z. Jia, H. Lv, Q. Liu, X. Tao, M. Liu, *AIP Adv.* **2018**, *8*, 015316.
[10] Y. Yao, R. Gangireddy, J. Kim, K. K. Das, R. F. Davis, L. M. Porter, *J. Vac. Sci. Technol., B: Nanotechnol. Microelectron.: Mater., Process., Meas., Phenom.* **2017**, *35*, 03D113.
[11] D. Splith, S. Müller, F. Schmidt, H. von Wenckstern, J. J. van Rensburg, W. E. Meyer, M. Grundmann, *Phys. Status Solidi A* **2014**, *211*, 40.
[12] M. Mohamed, K. Irmscher, C. Janowitz, Z. Galazka, R. Manzke, R. Fornari, *Appl. Phys. Lett.* **2012**, *101*, 132106.
[13] E. Farzana, Z. Zhang, P. K. Paul, A. R. Arehart, S. A. Ringel, *Appl. Phys. Lett.* **2017**, *110*, 202102.
[14] R. Suzuki, S. Nakagomi, Y. Kokubun, *Appl. Phys. Lett.* **2011**, *98*, 3.
[15] S. Müller, H. von Wenckstern, F. Schmidt, D. Splith, F. Schein, H. Frenzel, M. Grundmann, *Appl. Phys. Express* **2015**, *8*, 121102.
[16] T. Oshima, T. Okuno, N. Arai, N. Suzuki, S. Ohira, S. Fujita, *Appl. Phys. Express* **2008**, *1*, 011202.
[17] Q. He, W. Mu, H. Dong, S. Long, Z. Jia, H. Lv, Q. Liu, M. Tang, X. Tao, M. Liu, *Appl. Phys. Lett.* **2017**, *110*, 093503.
[18] M. Bartic, C.-I. Baban, H. Suzuki, M. Ogita, M. Isai, *J. Am. Ceram. Soc.* **2007**, *90*, 2879.
[19] R. Buzio, A. Gerbi, A. Gadaleta, L. Anghinolfi, F. Bisio, E. Bellingeri, A. S. Siri, D. Marrè, *Appl. Phys. Lett.* **2012**, *101*, 243505.
[20] M. W. Allen, S. M. Durbin, *Appl. Phys. Lett.* **2008**, *92*, 122110.
[21] C. Fares, F. Ren, S. J. Pearton, *ECS J. Solid State Sci. Technol.* **2019**, *8*, Q3007.
[22] J. H. Werner, H. H. Güttler, *J. Appl. Phys.* **1991**, *69*, 1522.
[23] A. Lajn, H. von Wenckstern, M. Grundmann, G. Wagner, P. Barquinha, E. Fortunato, R. Martins, *J. Appl. Phys.* **2013**, *113*, 044511.
[24] M. Prietsch, *Phys. Rep.* **1995**, *253*, 163.
[25] A. Gerbi, C. González, R. Buzio, N. Manca, D. Marrè, L. D. Bell, D. G. Trabada, S. Di Matteo, P. L. de Andres, F. Flores, *Phys. Rev. B* **2018**, *98*, 205416.
[26] K. G. Rana, S. Parui, T. Banerjee, *Phys. Rev. B* **2013**, *87*, 85116.
[27] R. Buzio, A. Gerbi, E. Bellingeri, D. Marré, *Appl. Phys. Lett.* **2018**, *113*, 141604.
[28] A. Gerbi, R. Buzio, A. Gadaleta, L. Anghinolfi, M. Caminale, E. Bellingeri, A. S. Siri, D. Marré, *Adv. Mater. Interfaces* **2014**, *1*, 1300057.
[29] T. C. Lovejoy, R. Chen, X. Zheng, E. G. Villora, K. Shimamura, H. Yoshikawa, Y. Yamashita, S. Ueda, K. Kobayashi, S. T. Dunham, F. S. Ohuchi, M. A. Olmstead, *Appl. Phys. Lett.* **2012**, *100*, 181602.
[30] R. Wakabayashi, M. Hattori, K. Yoshimatsu, K. Horiba, H. Kumigashira, A. Ohtomo, *Appl. Phys. Lett.* **2018**, *112*, 232103.
[31] R. T. Tung, *Appl. Phys. Rev.* **2014**, *1*, 011304.
[32] J. Yun, *Adv. Funct. Mater.* **2017**, *27*, 1606641.
[33] H. Galinski, T. Ryll, P. Reibisch, L. Schlagenhauf, I. Schenker, L. J. Gauckler, *Acta Mater.* **2013**, *61*, 3297.
[34] J. B. Varley, J. R. Weber, A. Janotti, C. G. Van de Walle, *Appl. Phys. Lett.* **2010**, *97*, 142106.
[35] L. Dong, R. Jia, B. Xin, B. Peng, Y. Zhang, *Sci. Rep.* **2017**, *7*, 40160.
[36] A. Y. Polyakov, N. B. Smirnov, I. V. Shchemerov, E. B. Yakimov, J. Yang, F. Ren, G. Yang, J. Kim, A. Kuramata, S. J. Pearton, *Appl. Phys. Lett.* **2018**, *112*, 032107.
[37] C. Baeumer, N. Raab, T. Menke, C. Schmitz, R. Rosezin, P. Müller, M. Andrä, V. Feyer, R. Bruchhaus, F. Gunkel, C. M. Schneider, R. Waser, R. Dittmann, *Nanoscale* **2016**, *8*, 13967.
[38] Z. Li, H. Li, Z. Wu, M. Wang, J. Luo, H. Torun, P. Hu, C. Yang, M. Grundmann, X. Liu, Y. Fu, *Mater. Horiz.* **2019**, *6*, 470.
[39] S. P. Arnold, S. M. Prokes, F. K. Perkins, M. E. Zaghloul, *Appl. Phys. Lett.* **2009**, *95*, 103102.
[40] Z. Zhang, E. Farzana, A. R. Arehart, S. A. Ringel, *Appl. Phys. Lett.* **2016**, *108*, 052105.
[41] M. Andrä, H. Bluhm, R. Dittmann, C. M. Schneider, R. Waser, D. N. Mueller, F. Gunkel, *Phys. Rev. Mater.* **2019**, *3*, 44604.
[42] M. Lübben, S. Wiefels, R. Waser, I. Valov, *Adv. Electron. Mater.* **2018**, *4*, 1700458.
[43] B. R. Tak, S. Dewan, A. Goyal, R. Pathak, V. Gupta, A. K. Kapoor, S. Nagarajan, R. Singh, *Appl. Surf. Sci.* **2019**, *465*, 973.
[44] D. Cooper, C. Baeumer, N. Bernier, A. Marchewka, C. La Torre, R. E. Dunin-Borkowski, S. Menzel, R. Waser, R. Dittmann, *Adv. Mater.* **2017**, *29*, 1700212.
[45] F. Messerschmitt, M. Jansen, J. L. M. Rupp, *Adv. Electron. Mater.* **2018**, *4*, 1800282.

[46] J. Lu, J. Xing, D. Chen, H. Xu, X. Han, D. Li, *J. Mater. Sci.* **2019**, *54*, 6530.
[47] J. Ma, H. J. Cho, J. Heo, S. Kim, G. Yoo, *Adv. Electron. Mater.* **2019**, *5*, 1800938.
[48] E. Swinnich, M. N. Hasan, K. Zeng, Y. Dove, U. Singisetti, B. Mazumder, J. H. Seo, *Adv. Electron. Mater.* **2019**, *5*, 1800714.
[49] J. Hou, S. S. Nonnenmann, W. Qin, D. A. Bonnell, *Appl. Phys. Lett.* **2013**, *103*, 252106.
[50] J. Kim, F. Ren, S. J. Pearton, *Nanoscale Horiz.* **2019**, *4*, 1251.
[51] R. Buzio, A. Gerbi, D. Marré, M. Barra, A. Cassinese, *J. Vac. Sci. Technol., B: Nanotechnol. Microelectron.: Mater., Process., Meas., Phenom.* **2016**, *34*, 41212.
[52] R. Buzio, A. Gerbi, D. Marrè, M. Barra, A. Cassinese, *Org. Electron.* **2015**, *18*, 44.
[53] B. A. Morgan, A. A. Talin, W. G. Bi, K. L. Kavanagh, R. S. Williams, C. W. Tu, T. Yasuda, T. Yasui, Y. Segawa, *Mater. Chem. Phys.* **1996**, *46*, 224.
[54] H. J. Im, B. Kaczer, J. P. Pelz, S. Limpijumnong, W. R. L. Lambrecht, W. J. Choyke, *J. Electron. Mater.* **1998**, *27*, 345.
[55] A. Chahboun, R. Coratger, F. Ajustron, J. Beauvillain, I. M. Dharmadasa, A. P. Samantilleke, *J. Appl. Phys.* **2000**, *87*, 2422.
[56] E. G. Brazel, M. A. Chin, V. Narayanamurti, D. Kapolnek, E. J. Tarsa, S. P. DenBaars, *Appl. Phys. Lett.* **1997**, *70*, 330.

